# *Magnetic field inversions at 1 AU: comparisons between mapping predictions and observations*

Article

Published Version

It is advisable to refer to the publisher's version if you intend to cite from the work.  See Guidance on citing.

## www.reading.ac.uk/centaur

# RESEARCH ARTICLE

**Key Points:**
- Predict magnetic field inversions by mapping field lines using a 2-D data-driven solar wind model with nonradial source magnetic field
- Compare predicted field inversions with 1 AU observations for five solar rotations at different phases of solar cycle 23
- Confirm persistence of inversions throughout the cycle and suggest most inversions originate at the wind's source surface or below

**Correspondence to:**
B. Li,
bo.li@sydney.edu.au

# Magnetic field inversions at 1 AU: Comparisons between mapping predictions and observations

**B. Li[1], Iver H. Cairns[1], M. J. Owens[2], D. Neudegg[3], V. V. Lobzin[1,3], and G. Steward[3]**

[1]School of Physics, University of Sydney, Sydney, New South Wales, Australia, [2]Space Environment Physics Group, Department of Meteorology, University of Reading, Reading, UK, [3]Space Weather Services, Bureau of Meteorology, Sydney, New South Wales, Australia

**Abstract** Large-scale magnetic field configurations are important for the transport of solar wind strahl electrons, which are suprathermal and directed along the field outward from the Sun. Strahl electrons are routinely used to infer not only the field configurations between the Sun and Earth but also local field structures, i.e., field inversions, where the magnetic field is locally folded back or inverted. Using solar wind data from ACE observations and a 2-D data-driven solar wind model with nonzero azimuthal magnetic field at the solar wind source surface, magnetic field lines are mapped between the Sun and Earth and beyond, in the solar equatorial plane. Standard verification metrics are used to assess, for five solar rotations at different phases of solar cycle 23, the performance of the mapping predictions for observed inversions, which are inferred from solar wind suprathermal electrons and magnetic fields measured by ACE. The probability of detection is consistently $\approx 0.70$ across the different phases. The success ratio, the Hanssen-Kuipers skill score, and the Heidke skill score are $\approx 0.55$–$0.70$ for the four rotations in the rising, solar maximum, and declining phases, but $\approx 0.35$–$0.60$ for the rotation near solar minimum, during which almost half of the samples have undetermined field configurations. Our analyses confirm the persistence of inversions throughout solar cycle 23, suggest for most observed inversions a solar/coronal origin at the wind's source surface or below, and predict that inversions should be less common for larger heliocentric distance $r \stackrel{>}{\sim} 3$ AU than for smaller $r$.

## 1. Introduction

Near-Earth solar wind observations of magnetic field and suprathermal electrons suggest that throughout the solar cycle large-scale magnetic field lines between the Sun and Earth are sometimes locally folded back or inverted [*Kahler et al.*, 1996, 1998; *Crooker et al.*, 1996, 2004b; *Owens et al.*, 2013]. These field inversions occur approximately 5% of the time in the ecliptic plane near 1 AU [*Kahler et al.*, 1998; *Owens et al.*, 2013] and are also reported at high latitudes [*Balogh et al.*, 1999].

In broad terms, field inversions occur in two categories: the more common short-duration inversions of 1–2 h [e.g., *Kahler et al.*, 1998; *Owens et al.*, 2013] and the less common long-duration inversions which may last more than half a day [*Crooker et al.*, 2004b; *Owens et al.*, 2013]. Physically, turbulent processes are proposed to be the cause of some short-duration inversions [*Owens et al.*, 2013], while interchange reconnection near the Sun within either a streamer or a pseudostreamer may produce the long-duration inversions [*Crooker et al.*, 2004b; *Owens et al.*, 2013]. In addition, long-duration inversions are interpreted to be 3-D in nature [*Crooker et al.*, 2004b]. Generally, inversions occur in slow wind [*Crooker et al.*, 2004b; *Owens et al.*, 2013], at the boundaries of opposite magnetic sectors, and within the sector boundaries (SBs) [e.g., *Kahler et al.*, 1996, 1998; *Crooker et al.*, 2004b; *Foullon et al.*, 2009; *Fazakerley et al.*, 2016]. Moreover, the inversion occurrence rates are found to be approximately constant throughout the period 1998–2011 [*Owens et al.*, 2013].

Independently, magnetic field lines directly traced by the sources of type III solar radio bursts sometimes show the presence of small-scale structures like kinks and inversions in the ecliptic plane [*Fainberg and Stone*, 1974; *Reiner et al.*, 1995]. Type III radio bursts are primarily produced by flare-accelerated electrons with speeds of 0.1–0.5 of the light speed; these electrons leave the Sun as beams into interplanetary space along the underlying magnetic field lines [e.g., *Suzuki and Dulk*, 1985].

The presence of field inversions at 1 AU has important implications in at least three respects:

1. Interpretation of the origin and transport of nonthermal solar particles. Field inversions can lead these particles to propagate sunward and hence appear not to be solar origin. These particles include solar wind suprathermal electrons, solar energetic particles (SEPs), and flare-accelerated electrons that produce type III solar radio bursts [e.g., *Suzuki and Dulk*, 1985; *Owens and Forsyth*, 2013].

2. Identification of the SB crossings. Due to the presence of inversions, changes in magnetic field polarities do not necessarily signal the transition from one sector to another [*Kahler and Lin*, 1995; *Crooker et al.*, 2004b], although they do indicate the presence of heliospheric current sheets or localized current sheets or both [e.g., *Kahler et al.*, 1996; *Crooker et al.*, 1996; *Szabo et al.*, 1999; *Foullon et al.*, 2009; *Owens et al.*, 2013; *Liu et al.*, 2014]. Therefore, SB crossings cannot be unambiguously identified by directional changes in the magnetic field **B** alone. Additional observations of solar wind suprathermal electrons help to remove the ambiguities [*Kahler and Lin*, 1994, 1995]. This is because the solar wind electrons are almost always characterized by an antisunward component directed along the magnetic field, the so-called "strahl" or "heat-flux" electrons [*Feldman et al.*, 1975; *Rosenbauer et al.*, 1977]. In fact, pitch angle distributions (PADs) of the field-aligned strahl electrons near Earth are routinely used to infer the true polarities of the source magnetic fields [e.g., *Gosling et al.*, 1987; *Kahler et al.*, 1996; *Neugebauer*, 2008; *Liu et al.*, 2014] and the existence of inversions [*Kahler et al.*, 1998; *Owens et al.*, 2013].

3. Estimation of the total magnetic flux at the solar wind's source surface. The estimation is important for assessing the reconstructed flux from geomagnetic activity indices [*Lockwood et al.*, 2014]. Field inversions contribute to the observed increase of the total magnetic flux with heliocentric distance $r$ [e.g., *Owens et al.*, 2008; *Lockwood et al.*, 2009; *Erdős and Balogh*, 2014]. Consequently, accurate deduction of the total magnetic flux at the source surface from in situ magnetic field observations requires careful removal of the excess flux, as reviewed by *Lockwood* [2013] and *Owens and Forsyth* [2013].

The presence of fine temporal and spatial scale inversion structures on global magnetic field lines cannot be understood within the standard picture of the Parker spiral [*Parker*, 1958]. Nonetheless, the observed solar wind magnetic field averaged over many solar rotations [e.g., *Thomas and Smith*, 1980; *Burlaga and Ness*, 1993] and some observations of type III radio sources [e.g., *Fainberg et al.*, 1972; *Reiner et al.*, 1995; *Li et al.*, 2016b] are closely Parker spiral like. Observations indicate that at inversions the in-ecliptic magnetic field angle $\phi_B$ tends to cluster around 45° and 225° [*Kahler et al.*, 1998; *Crooker et al.*, 2004b], where $\phi_B = \tan^{-1}(B_\phi/B_r)$, $B_\phi$ and $B_r$ are the azimuthal and radial components, respectively, of the magnetic field in the geocentric solar ecliptic (GSE) coordinate system. These two particular angles, however, are inconsistent with the standard Parker spiral model, which formally applies to the ranges of 90°–180° and 270°–360°.

Recently, we have developed an approach for mapping magnetic field lines in the solar equatorial plane between the Sun and Earth and beyond [*Li et al.*, 2016a]. Our approach can predict, in principle, both fine-scale field structures like inversions and large-scale field configurations of both open and closed field lines for all values of $\phi_B$. This approach uses a solar wind magnetic field model driven by observations of near-Earth solar wind magnetic field and velocity [*Schulte in den Bäumen et al.*, 2011, 2012]. The model assumes that the azimuthal magnetic field at the source surface is nonzero but otherwise contains almost the same ingredients as the standard Parker spiral model. Our approach has been validated using the observed time-varying PADs of solar wind suprathermal electrons at 1 AU [*Li et al.*, 2016a] and successfully applied to a type III radio burst whose source path is well predicted by our mapping [*Li et al.*, 2016b]. Interestingly, local field line inversions are predicted by both works [*Li et al.*, 2016a, 2016b] and near both minimum and maximum solar activity [*Li et al.*, 2016a].

This work specifically applies our magnetic mapping approach to the field line inversions observed by *Owens et al.* [2013]. We study the field inversions predicted by our mapping and compare them with observations for five solar rotations across the different phases of solar cycle 23, between May 1998 and July 2008. In sections 2 and 3 the approaches for mapping magnetic field lines [*Li et al.*, 2016a] and for observational detection of field inversions [*Owens et al.*, 2013] are reviewed, respectively. Verification metrics used in assessing the performance of our mapping predictions for inversion events are outlined in section 4. Section 5 reports the field inversions predicted for the mapped field lines and the associated comparisons with the observations. Section 6 discusses the results and draws the conclusions.

## 2. Magnetic Field Mapping

*Li et al.* [2016a] proposed a two-step approach for mapping the magnetic field lines in the solar equatorial plane for a given starting point $\mathbf{r}_0 = (x_0, y_0)$ located between the Sun and Earth. First, the point $\mathbf{r}_0$ is advanced to a new point $\mathbf{r} = (x, y)$ along the direction of the local magnetic field:

$$x = x_0 + \mathrm{d}x, \tag{1}$$

$$y = y_0 + \mathrm{d}y, \tag{2}$$

where

$$\mathrm{d}x = \frac{1}{4} \sum_{i=1}^{4} \frac{B_{xi}}{B_i} \mathrm{d}l, \tag{3}$$

$$\mathrm{d}y = \frac{1}{4} \sum_{i=1}^{4} \frac{B_{yi}}{B_i} \mathrm{d}l, \tag{4}$$

are the field direction-weighted averages of four grid points $\mathbf{r}_i$ with corresponding $\mathbf{B}_i(\mathbf{r}_i) = (B_{xi}, B_{yi})$, $B_i = |\mathbf{B}_i(\mathbf{r}_i)|$, and $\mathrm{d}l$ is the stepsize. These four grid points form the smallest 2-D grid cell enclosing the point $\mathbf{r}_0$. The process is repeated until the desired radial distance from the Sun or Earth is reached. Second, the point $\mathbf{r}_0$ is advanced in the direction opposite to the local magnetic field until the desired ending distance is reached, similar to the first step.

In order to obtain the desired magnetic field line map, the above two steps are repeated for all chosen starting points in the equatorial plane. The above mapping does not explicitly satisfy the divergence-free condition $\nabla \cdot \mathbf{B} = 0$, as discussed further in section 6. Each mapped field line is first visually examined to identify its configuration out of the four types: (i) open antisunward, (ii) open sunward, (iii) loop rooted to the Sun, and (iv) loop disconnected from the Sun. The open field lines are subsequently inspected to determine if they have inversions at 1 AU. Specifically, an inversion is identified on an open field line if the field line crosses the circle of radius 1 AU 3 times (or a larger odd number of times) instead of once. The generalization for identifying inversions at another heliocentric distance is obvious. Occasionally, a field configuration is "undetermined" when the mapping is incomplete for a given starting point; the associated field line is then classified as "no inversion."

The magnetic field components on the right-hand sides of (3) and (4) are predicted using the model of *Schulte in den Bäumen et al.* [2011, 2012] and near-Earth solar wind data. The model applies in and near the solar equatorial plane. It assumes that both the solar wind sources and the solar wind itself are constant over one solar rotation (27 days) and that the wind varies with respect to the heliocentric distance $r$ and the longitude $\phi$ in general (except for the wind velocity $\mathbf{V}$ which varies with $\phi$ only) as a fixed pattern that rotates with the Sun and flows past Earth and beyond. Distinct from the usual Parker spiral model [*Parker*, 1958], the model of *Schulte in den Bäumen et al.* [2011, 2012] assumes that at the source surface $\mathbf{r}_s = (r_s, \phi_s)$ the $\mathbf{B}$ field has both $B_r$ and $B_\phi$ components, where $B_\phi(\mathbf{r}_s)$ may originate from solar dynamo effects and granulation cells (e.g., *Jokipii and Kota* [1989], the review by *Solanki et al.* [2006, and references therein], and *Schulte in den Bäumen et al.*, 2011]) as well as other solar phenomena like reconnection. Consequently, at any arbitrary location $\mathbf{r} = (r, \phi)$ with $r > r_s$,

$$B_r(r, \phi) = \frac{r_s^2}{r^2} B_r\left(r_s, \phi_s\right), \tag{5}$$

$$B_\phi(r, \phi) = \frac{r_s}{r} B_\phi\left(r_s, \phi_s\right) - \frac{\Omega\left(r - r_s\right)}{V\left(\phi_s\right)} B_r(r, \phi), \tag{6}$$

assuming that the wind flow is radial at a constant speed $V(\phi_s)$, where $\Omega$ is the angular speed of solar rotation at the equator and $\phi = \phi_s + (r - r_s)\Omega/V(\phi_s)$. Equation (5) is derived from $\nabla \cdot \mathbf{B} = 0$ by neglecting the azimuthal component, while (6) follows from $\nabla \times \mathbf{E} = 0$ and the frozen-in assumption. Further discussion of the assumptions is deferred to section 6.

**Table 1.** Contingency Table for Inversion Observations and Predictions

| | | Observed | |
|---|---|---|---|
| | | Inversion | No Inversion |
| Predicted | Inversion | Hit (TP) | False Alarm (FP) |
| | No Inversion | Miss (FN) | True Negative (TN) |

Practically, we first apply hourly averaged **B** and **V** data observed at $\mathbf{r}_{obs} = (r_{obs}, \phi_{obs})$ to (5) and (6) to extract $B_r(\mathbf{r}_s)$ and $B_\phi(\mathbf{r}_s)$ at the source surface, using

$$B_r (r_s, \phi_s) = \frac{r_{obs}^2}{r_s^2} B_r (r_{obs}, \phi_{obs}) . \tag{7}$$

$$B_\phi (r_s, \phi_s) = \frac{r_{obs}}{r_s} \left[ B_\phi (r_{obs}, \phi_{obs}) + \frac{\Omega (r_{obs} - r_s)}{V(\phi_s)} B_r (r_{obs}, \phi_{obs}) \right] . \tag{8}$$

The quantities $B_r(\mathbf{r})$ and $B_\phi(\mathbf{r})$ for $r > r_s$ are then predicted by substituting (7) and (8) into (5) and (6), as in the works by *Schulte in den Bäumen et al.* [2012] and *Li et al.* [2016a, 2016b]. It is assumed here that the solar wind conditions observed in the ecliptic plane with $r_{obs} \approx 1$ AU by the ACE spacecraft are the same as those in the solar equatorial plane and that the source surface is at the photosphere.

## 3. Observational Detection of Field Inversions

As detailed by *Owens et al.* [2013], field inversions are automatically identified using 64 s measurements of solar wind suprathermal electrons at 272 eV and magnetic fields from the ACE spacecraft, and the detection results are reported at hourly intervals. The automatic detection made it feasible for the statistical study of field inversions over a period of $\approx 14$ years [*Owens et al.*, 2013]. PAD classes are first identified using an automatic technique that compares the suprathermal electron fluxes parallel and antiparallel to the magnetic field with the background fluxes at all angles, using a threshold of a factor 2 above the background. Three PAD classes were identified, including strahls parallel to the field, strahls antiparallel to the field, and counterstreaming strahls (or bidirectional electrons, BDEs). Correspondingly, the field configurations were identified as open antisunward field lines, open sunward field lines, and loops with both ends connected to the Sun. For periods that neither the parallel strahl nor the antiparallel strahl exceeds the threshold, the field configurations were classified as undetermined [*Owens et al.*, 2013] and here are treated as "no inversion" events.

The above automatic identifications of PAD classes and the associated field inversions are sometimes likely to predict results that are different from those obtained by visual identification, a technique commonly used for short periods of times [e.g., *Gosling et al.*, 1987; *Crooker et al.*, 2004a]. For example, a spot check of inversions for part of Carrington rotation (CR) 1964 shows that the automatic identification detected 40 samples correctly and 3 samples incorrectly, and missed 7 inversions. Thus, for this period the automatic identification has a success rate of 80% and a missed detection rate about 15%. Such differences are not expected to significantly affect the results in this work.

## 4. Prediction Assessment

The performance of our mapping predictions for inversion events is assessed by using categorical verification metrics, which are calculated from a contingency table for dichotomous predictions [e.g., *Woodcock*, 1976; *Stanski et al.*, 1989]. The contingency table for inversion observations and predictions is shown in Table 1; it has four basic elements: the number of hits (true positives, TP), false alarms (false positives, FP), misses (false negatives, FN), and correct negatives (true negatives, TN). The number of observed inversion events is TP + FN, the number of observed noninversion events is FP+TN, and the total number of events ($N$) is the sum of all four elements.

The following standard verification metrics are employed for the relatively rare field inversion events and the more common noninversion events. The probability of detection (POD) is the fraction of the observed events that are correctly predicted:

$$\text{POD} = \frac{\text{TP}}{\text{TP} + \text{FN}} . \tag{9}$$

The success ratio (SR) calculates the fraction of the predicted events that is observed:

$$SR = \frac{TP}{TP + FP} . \tag{10}$$

The accuracy of the prediction when correct negatives are excluded from consideration can be shown by the threat score (TS) or critical success index:

$$TS = \frac{TP}{TP + FN + FP} . \tag{11}$$

The POD, SR, and TS all range from 0 to 1, with 0 for no skill and 1 for a perfect score.

Another metric is the false alarm ratio (FAR). This is the fraction of predicted events that actually do not occur; thus, FAR = 1-SR. The bias score (BS) is often used as a diagnostic to measure the ratio of the forecast events to the observed events:

$$BS = \frac{TP + FP}{TP + FN} , \tag{12}$$

although it does not quantify the correspondence between predictions and observations. A forecast tends to underforecast when BS<1 or overforecast when BS>1.

Skill scores measure the prediction accuracy relative to some reference prediction. The Hanssen-Kuipers skill score (HK), also called the true skill statistics or Peirce skill score, shows how well the prediction separates the "inversion" events from the "no inversion" events relative to random prediction:

$$HK = \frac{TP}{TP + FN} - \frac{FP}{FP + TN} . \tag{13}$$

The Heidke skill score (HSS) represents the accuracy of the prediction relative to that of random chance:

$$HSS = \frac{(TP + TN) - A}{N - A} , \tag{14}$$

where

$$A = \frac{1}{N}[(TP + FN)(TP + FP) + (TN + FN)(TN + FP)] \tag{15}$$

estimates the number of true events expected by chance. Both HK and HSS have 1 for perfect predictions, 0 for no skill, and <0 for worse performance than the random prediction.

## 5. Results

This section compares the small-scale inversions at 1 AU and large-scale configurations of the magnetic field lines predicted by our mapping approach for five solar rotations in various phases of solar cycle 23 with those observed by *Owens et al.* [2013] using solar wind suprathermal electron and magnetic field data. The focus is on local field inversions, with detailed study for CR 1964, which was demonstrated in *Owens et al.* [2013]. Table 2 summarizes the mapping predictions for inversions and the associated verification metrics. Note that this paper uses the Bartels rotation length of 27 days, so the start and end times for each solar rotation differ slightly from the corresponding Carrington rotation of 27.2753 days.

### 5.1. CR 1964
Carrington rotation 1964, from 13 June to 10 July 2000, near solar maximum, was found to have one of the highest occurrence rates of field inversions during the whole 1998–2011 period [*Owens et al.*, 2013]. It thus offers a very good opportunity to compare in detail the structures of our predicted field lines with the observations.

### 5.1.1. The Solar Wind
Figure 1 shows hourly solar wind data from ACE between 13 June and 9 July 2000. The PAD and magnetic field data show that on large scales with duration longer than 1 day this rotation has a two-sector structure, with SBs near 22 June and 4 July. During this rotation, the solar wind was perturbed by many interplanetary coronal mass ejections (ICMEs) [*Richardson and Cane*, 2010], as marked in fouth and fifth panels.

**Table 2.** Summary of Performance Results for Inversion Events for Five Carrington Rotations in Solar Cycle 23, Using 1 h Samples[a]

| | | Carrington Rotation in Solar Cycle 23 | | | | |
|---|---|---|---|---|---|---|
| | | Rising | | Solar Maximum | Declining | Solar Minimum |
| | | CR 1936 | CR 1947 | CR 1964 | CR 2016 | CR 2071 |
| Contingency Table | TP | 52 (84) | 44 (51) | 54 (85) | 37 (63) | 24 (66) |
| | FP | 40 (8) | 18 (11) | 35 (4) | 30 (4) | 47 (5) |
| | FN | 29 | 15 | 19 | 16 | 11 |
| | TN | 527 [24%] | 571 [12%] | 540 [19%] | 565 [20%] | 566 [45%] |
| Performance Result | POD | 0.64 (0.74) | 0.75 (0.77) | 0.74 (0.82) | 0.70 (0.80) | 0.69 (0.86) |
| | SR | 0.57 (0.91) | 0.71 (0.82) | 0.61 (0.96) | 0.55 (0.94) | 0.34 (0.93) |
| | TS | 0.43 (0.69) | 0.57 (0.66) | 0.50 (0.79) | 0.45 (0.76) | 0.29 (0.80) |
| | FAR | 0.43 (0.09) | 0.29 (0.18) | 0.39 (0.04) | 0.45 (0.06) | 0.66 (0.07) |
| | BS | 1.14 (0.81) | 1.05 (0.94) | 1.22 (0.86) | 1.26 (0.85) | 2.03 (0.92) |
| | HK | 0.57 (0.73) | 0.72 (0.75) | 0.68 (0.81) | 0.65 (0.79) | 0.61 (0.85) |
| | HSS | 0.54 (0.79) | 0.70 (0.77) | 0.62 (0.86) | 0.58 (0.85) | 0.41 (0.88) |

[a]The values in parentheses are obtained by assuming that at the times of predicted inversions the undetermined field configurations from the observations are indeed inversions. (The values of FN and TN are not affected by this assumption.) The percentage values in square brackets after TN indicate for each rotation the percentages of the total undetermined field configurations from observations, which are treated as no inversion events.
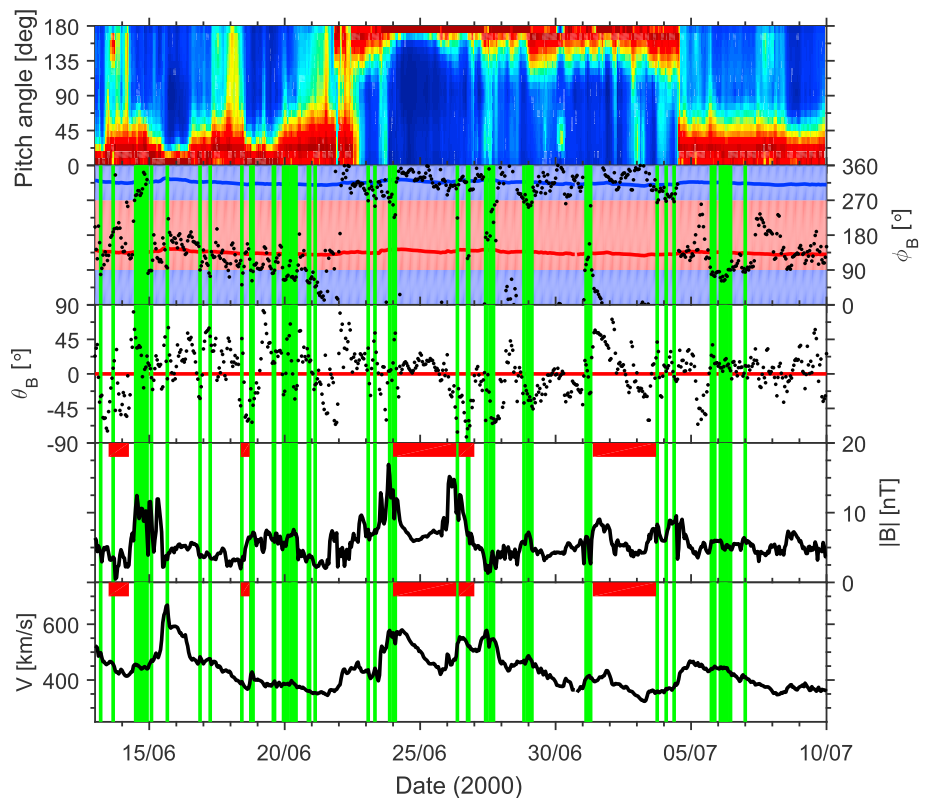


**Figure 1.** ACE observation of the solar wind for CR 1964 between 13 June and 9 July 2000. (first to fifth panels) Normalized 272 eV electron pitch angle distribution, the in-ecliptic and out-of-ecliptic magnetic field angles in GSE coordinates, the total magnetic field, and radial solar wind speed. The red and blue shaded regions in Figure 1 (second panel) show sunward and antisunward hemispheres, respectively. Green vertical lines show the inverted flux regions [*Owens et al.*, 2013]. Red horizontal bars near the top of Figure 1 (fourth and fifth panels) show the periods of ICMEs identified by *Richardson and Cane* [2010].
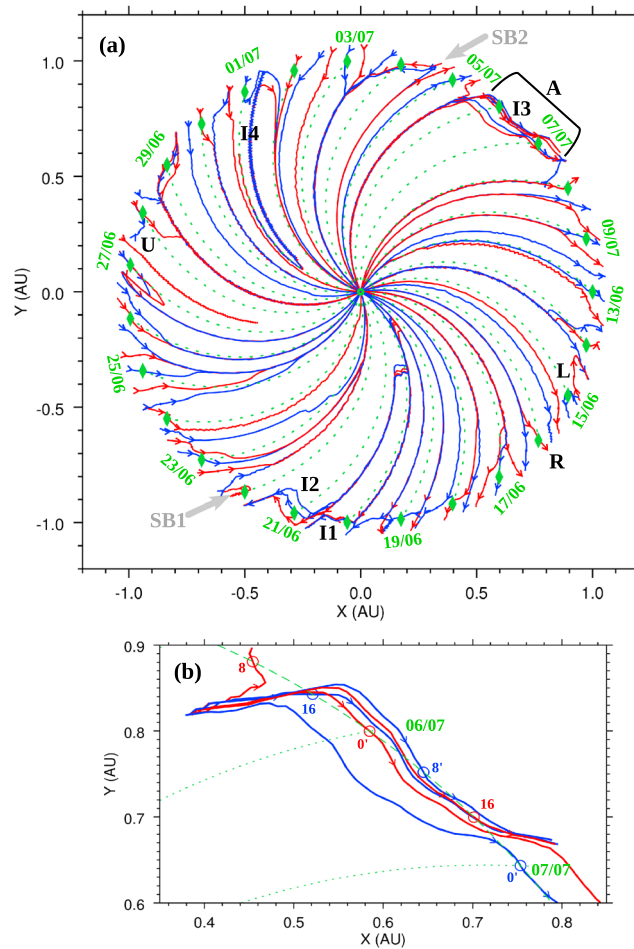
**Figure 2.** (a) Predicted map of magnetic field lines for CR 1964. The Sun is at the center, and the Earth appears to move clockwise around the Sun, with green diamonds showing Earth's longitudinal locations at 0000 UT on each day. Dotted green curves starting from the Sun, and passing through the diamonds are Parker spirals, which are predicted using the averaged radial solar wind speed for the entire rotation. The starting points for the mapping are spaced at 8 h intervals around Earth's orbit each day, starting from 0000 UT on 13 June 2000. Field lines are alternately colored blue and red to ease visualization, with arrows indicating the field directions. The black labels L, R, I1, etc. (with black bracket for label A) are discussed in section 5.1.2. Sector boundaries identified using hourly magnetic field data are marked with gray arrows. (b) Snapshot of the field lines in Figure 2a between 5 and 7 July near 1 AU. To aid visual identifications of field line inversions at 1 AU, Earth's orbit is drawn (dashed green circular arc), and the mapping starting points are marked by circles, where the UT hours are shown by numerals with primed numerals indicating inversions at 1 AU.

### 5.1.2. The Magnetic Map and General Features

Figure 2a shows the predicted map of magnetic field lines for this rotation. The field lines are mapped from starting points that are located at 1 AU, separated in longitude by an angle corresponding to 8 h, and begin at 0000 UT each day. The map shows that on the large scale of one rotation, the two-sector structure as indicated by the **B** and PAD data in Figure 1 is clearly seen. Examining the map on the intermediate scale of days shows that the field lines are mostly open. Only on one occasion, the period of 14–15 June are loops disconnected from the Sun predicted (labeled L). Figure 2a also shows that for the starting points at 0800 UT and 1600 UT on 27 June (labeled U), the mapping is incomplete with undetermined field configurations. This occurs because localized fluctuations in the orientation of the **B** vector cause the mapping to proceed extremely slowly toward the Sun, in fact, not reaching the Sun [*Li et al.*, 2016a].

The predicted open field lines in Figure 2a are not, in general, closely Parker spiral like for sufficiently large $r \gtrsim 0.4$ AU. The nonspiral structures include those with strong azimuthal orientations (e.g., during the period of 5–7 July near Earth's orbit, labeled A), radial orientations (e.g., the red field line starting at 0000 UT on 16 June near Earth's orbit, labeled R), and inversions. Examples of inversions include the three periods on 20 June (labeled I1), during 20–21 June (labeled I2), and during 5–7 July (labeled I3), where the field lines are sunward locally near Earth's orbit but are open antisunward on larger scale. Another example of

inversion is on 1 July (labeled I4), where the field lines are topologically open sunward while being inverted either locally near 1 AU (for the starting point at 0000 UT) or on large $r$ ($\approx 0.7$ AU) scale (for the starting points at 0800 UT and 1600 UT). Figure 2a also shows that even when field lines are locally inverted, the majority of these field lines still follow the corotation direction (e.g., I1–I3) and rarely are directed opposite to the corotation direction (only I4). Figure 2b shows a close-up of the field lines between 5 and 7 July, in order to demonstrate clearly the predicted inversions at 1 AU. The presence of such non-Parker-like field structures in Figure 2 is consistent with the results found for other solar rotations near both solar minimum and solar maximum [*Li et al.*, 2016a, 2016b].

### 5.1.3. Small-Scale Field Inversions

Figure 3 shows a close-up map of predicted field lines as functions of longitude and heliocentric distance near Earth's orbit, to better illustrate field line inversions at 1 AU for CR 1964. For visual clarity, the field lines
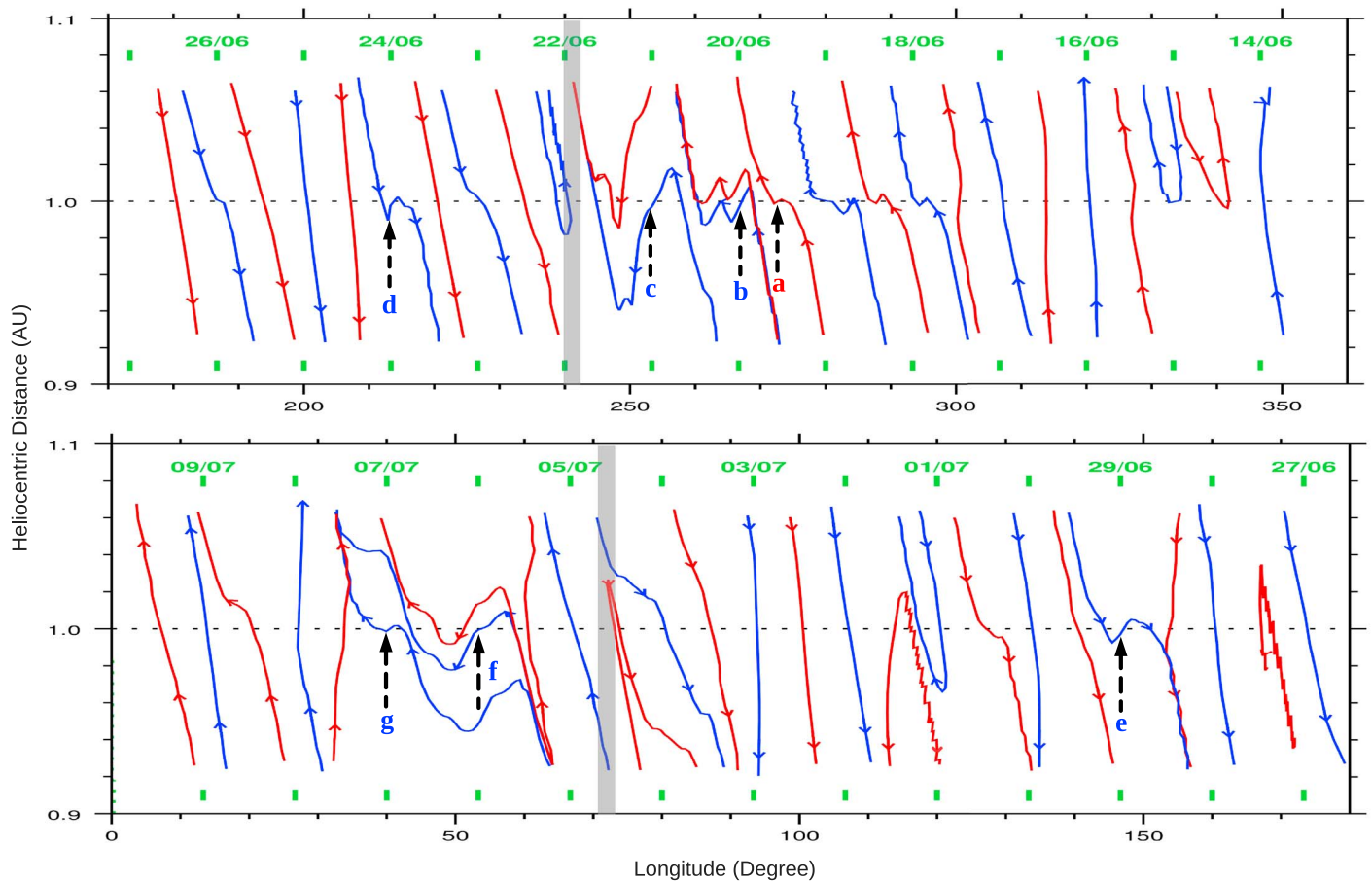
**Figure 3.** Mapped magnetic field lines as functions of longitude and heliocentric distance for CR 1964 near Earth's orbit. The starting points for the mapping are at 1 AU and at longitudes corresponding to 0000 UT (blue) and 1200 UT (red) each day, beginning from 14 June 2000. Green bars show the longitudinal locations of 0000 UT on each day. Dashed black arrows indicate inverted field lines at 1 AU at either 0000 UT or 1200 UT, labeled by "a"–"g" with colors same as the corresponding field lines. Shaded gray regions represent approximately the sector boundaries identified using the hourly magnetic field data.

in Figure 3 are mapped at 0000 UT and 1200 UT each day, i.e., at 12 h intervals that are longer than Figure 2's 8 h intervals, but with otherwise identical conditions.

We see from Figure 3 that field lines are locally inverted in the vicinity of 1 AU during 17–21 June, around 24 and 29 June, and during 5–7 July. The two field lines starting on 1 July are inverted as well, although one appears to be a disconnected loop and the other a connected loop, due to the finite $r$ range of Figure 3. Among these inverted field lines, only seven of them are inverted at 1 AU, with six inversions occurring at 0000 UT and one inversion at 1200 UT. (Figure 3 also shows other features of the predicted field lines, e.g., disconnected loops around 15 June and radial fields around 0000 UT and 1200 UT on 16 June, consistent with Figure 2.)

### 5.1.3.1. Performance Metrics

In order to quantitatively assess the capability of our mapping approach for predicting the inversions observed by *Owens et al.* [2013], Figure 4 shows the timings of field inversions inferred from the PAD and **B** field observations [*Owens et al.*, 2013] and predicted by a magnetic field map (not shown) with starting points at hourly (rather than 8 h) intervals but otherwise identical conditions to Figure 2. We see that our mapping approach predicts most of the observed inversions, although it does miss those observed on 14, 15, and 27 June. Our mapping (cf. Figure 2) predicts instead disconnected loops on 14 and 15 June, and undetermined field configurations on 27 June (due to directional fluctuations in the local magnetic field on 27 June).

Quantitatively, Figure 4 and Table 2 show that out of a total of 73 inversions (11% of the total samples) observed by ACE our mapping predicts 54 (=TP) inversions that are consistent with the observations, and so 74% (=POD) of the observed inversions are predicted correctly with 19 (=FN) misses. The prediction has false alarms, with FP = 35, so that 61% (=SR) of the predicted inversions are observed. Moreover, a threat score of
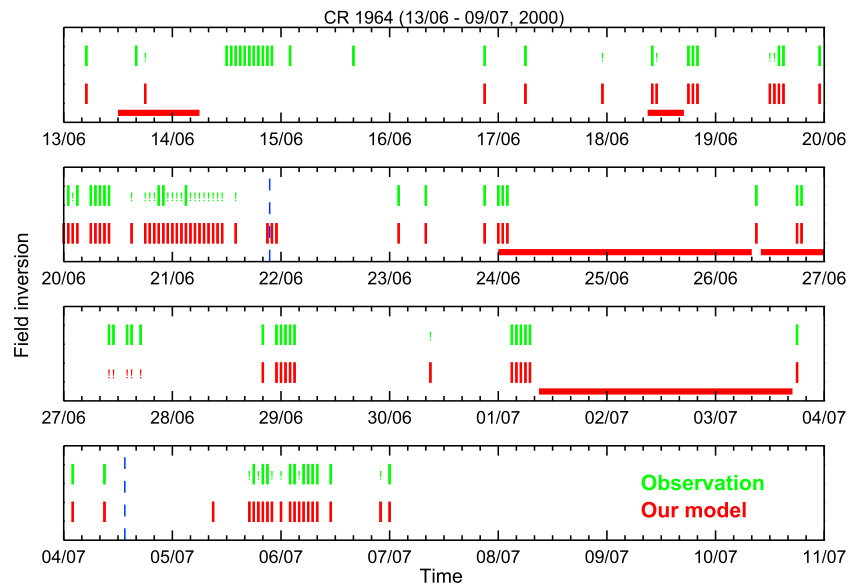
**Figure 4.** Comparison for CR 1964 of the times of field line inversions inferred from PAD and magnetic field observations (green bars) and with those predicted by our mapping (red bars), where the mapping has starting points spaced at hourly intervals but otherwise identical conditions to Figure 2. Also shown with green (red) exclamation marks are the times when field configurations cannot be determined from the observations (predictions), while the predictions (observations) show inversions. Dashed vertical blue lines mark sector boundaries identified using hourly magnetic field data. Red horizontal bars near the bottom of each panel show the periods of the ICMEs identified by *Richardson and Cane* [2010].

TS = 0.50 is achieved so half of the inversion events that are either observed and/or predicted are correctly predicted. In addition, the two skill scores are HK = 0.68 and HSS = 0.62, so our prediction is nearly 70% better in separating the inversion events from the no inversion events and over 60% better in accuracy than random predictions. Finally, the mapping slightly overpredicts the inversion events, with BS = 1.22.

### 5.1.3.2. Effects of the Undetermined Field Configurations

Notably, Figure 4 also shows that our mapping sometimes predicts longer-lasting inversion events than observed. Examples include the predicted 18 h long 20–21 June event and the 5 July event lasting 6 h. Observationally, the 20–21 June period has 3 samples with inversions and 15 samples with unknown field configurations, while for the 5 July period, 3 samples have inversions, and 3 samples are undetermined.

For CR 1964, there are a total of 125 (i.e., 19%, see Table 2) samples with observationally undetermined field configurations, 31 of which correspond to inversions predicted by the mapping (see Figure 4). If these 31 observational samples are assumed to be inversions, Table 2 shows that the predictions then have an upper limit of POD = (54 + 31)/(73 + 31) = 81.7% and so over 80% of the observed inversions are mapped correctly. The HK and HSS scores are then 81% and 86%, respectively, so improved by 19% and 39%, respectively, from those without such an assumption. Correspondingly, FAR = 0.04 (or SR = 0.96) and so indicates that less than 5% of the mapped inversion events are not observed. This assumption may not be unreasonable, considering (i) the very good agreement in sample timing between the predictions and the observations except for 14–15 and 27 June and (ii) the spot check, which shows that the automatic identification technique primarily misses events rather than incorrectly detects events (see section 3).

### 5.1.3.3. Effects of Varying Sample Interval

We see from Figure 4 that the observed inversions occurred sporadically but not evenly throughout the rotation, so it is expected that comparisons at intervals longer than the observed 1 h interval will yield different results in general. For example, for the map in Figure 2 with the starting points spaced by 8 h intervals and the first starting point at 0000 UT on 13 June, POD = 0.67 is found and so the observed inversions are correctly predicted 7% worse than that when hourly samples are compared. Thus, for CR 1964 varying the sampling interval has some, yet not significant, effects on the rate and accuracy of the predictions.

### 5.1.3.4. Association With Solar Wind Conditions

Figure 4 shows that both the observed and predicted inversions, either brief or long lasting, occurred within the large-scale magnetic sectors throughout the rotation, except for the predicted inversions at the SB on
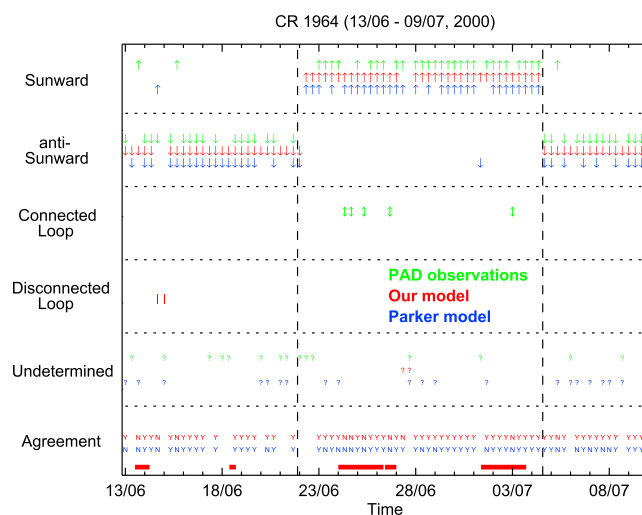
**Figure 5.** Comparisons for CR 1964 of field line configurations predicted by our model in Figure 2 (red) or Parker's model (blue) with those inferred from PAD observations (green). (first to fourth panels) The different field configurations. (fifth panel) Cases when field configurations cannot be determined. (sixth panel) Consistency check, with "Y" for agreement and "N" for disagreement. Dashed vertical black lines mark sector boundaries identified using hourly magnetic field data. Red horizontal bars near the bottom of Figure 5 (sixth panel) show the periods of the ICMEs identified by *Richardson and Cane* [2010].

21 June. Our inversion results are thus not inconsistent with the proposal that inversions are associated with interchange reconnection events at the Sun [*Crooker et al.*, 2004b; *Owens et al.*, 2013].

In addition, we see from Figure 4 that the predicted inversions correlate poorly with ICMEs, as inversions exist only occasionally when ICMEs are present. This result is consistent with previous observations that the majority of inversions are not associated with BDEs [*Kahler et al.*, 1998], which are an important signature of ICMEs [e.g., *Gosling et al.*, 1987; *Zurbuchen and Richardson*, 2006].

### 5.1.4. Large-Scale Field Configurations

In addition to assessing our field inversion predictions, here we assess also the predicted field configurations by using the time-varying classes of suprathermal electron PADs [*Li et al.*, 2016a]. Figure 5 compares the magnetic field configurations predicted by the map in Figure 2 (in red), obtained from the PAD observations (in green) [*Owens et al.*, 2013], and predicted by Parker's spiral model (in blue).

Figure 5 shows that the map predicts open antisunward field lines starting from the beginning of the rotation until the end of 22 June, with two disconnected loops lying within this period of time. Subsequently, the mapped field lines are open and directed sunward until near midday on 4 July, with a total of 35 such sampled field lines. On 27 June, there are two samples with unknown configurations, due to the incompleteness of the mapping already discussed for Figure 2. From midday on 4 July until the end of the rotation all the mapped field lines are directed antisunward. Figure 5 also shows that the observed fields are mostly (75.3%) open, there are five loops with both ends connected to the Sun, and the remainder (18.5%) are observationally undetermined [*Owens et al.*, 2013]. According to *Richardson and Cane* [2010], the two ICMEs during 24–27 June are associated with BDEs, while the 1–3 July ICME is not associated with BDEs, so suggesting the presence and absence, respectively, of connected loops. Slightly different from the results of *Richardson and Cane* [2010], the automatic technique by *Owens et al.* [2013] also identified one connected loop at 0000 UT on 3 July associated with the 1–3 July ICME, as shown in Figure 5. Our mapping predicts none of the observed connected loops; nevertheless, the results at the bottom of Figure 5, encompassing all field configurations, show that our mapping agrees at the 84.8% level with the observations.

Figure 5 also shows that according to Parker's model most field lines are open, with 30 samples being antisunward directed and 31 samples being sunward directed. The field configurations for the remainder (24.7%) cannot be predicted by Parker's model, since the observed magnetic azimuthal angle $\phi_B$ was within the ranges 0°–90° or 180°–270°, which do not fit within the framework of Parker's spiral model. An overall assessment shows that Parker's prediction agrees at the 69.7% level with the observations. Therefore, Figure 5 clearly shows that our model (with 85% agreement) works better than Parker's model for this rotation. This result is consistent with our previous work for two other solar rotations [*Li et al.*, 2016a].

In addition, for the hourly mapping used in Figure 4 for studying field inversions, our predictions and Parker's model predictions agree with the field configurations inferred from the PAD data at 81.5% and 63.7% levels, respectively. Both results are different from yet only lower by <6% than, those for the 8 h interval case discussed above in detail regarding Figure 5. Therefore, variation in the sampling rate leads to relatively small effects for studies of the CR 1964 field configurations.
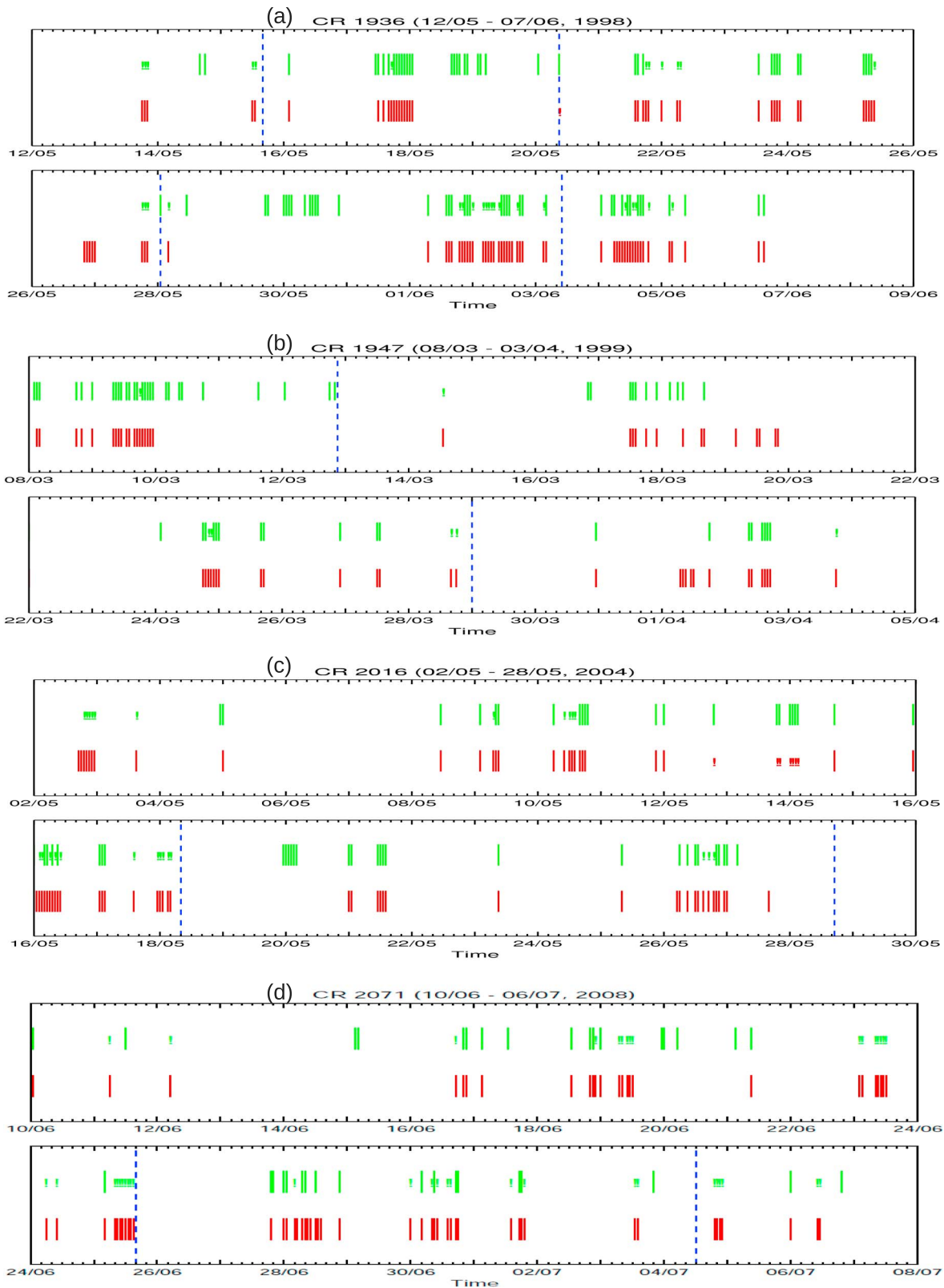
**Figure 6.** Comparisons for (a) CR 1936, (b) CR 1947, (c) CR 2016, and (d) CR 2071, of the times of field line inversions inferred from PAD and magnetic field observations (green) with those predicted by our mapping (red), in a format similar to Figure 4.

### 5.2. CR 1936, CR 1947, CR 2016, and CR 2071

This subsection studies the small-scale field inversion structures for four solar rotations representative of the rising (CR 1936 and CR 1947), declining (CR 2016), and solar minimum (CR 2071) phases of solar cycle 23. Inversions are now predicted for these rotations, using the same approach as for CR 1964. Figure 6 compares the inversion sample timings obtained from the mapping predictions with the observations [*Owens et al.*, 2013], and Table 2 shows the performance of our mapping predictions.

#### 5.2.1. Performance Metrics

Figure 6a shows that for CR 1936 during the rising phase of solar cycle 23, inversions are observed for 1/8 of the hourly samples, i.e., 81 inversions. Quite often, the observed inversions last 4 h or more; examples include those on 17–18 May, 30 May, and 2 June. In comparison, Table 2 shows that our mapping predicts a total of 92 inversions with 52 (=TP) of them consistent with the observations, and so has POD = 0.64, SR = 0.57, HK = 0.57, and HSS = 0.54. The incorrectly predicted timings include periods during 29–30 and 18–19 May, for which disconnected loops are predicted but inverted open antisunward fields are observed, and periods during 26–27 May when inverted open sunward field lines are predicted but sun-connected loops are observed.

Figure 6b shows that for CR 1947 inversions are observed to occur less often, and most of them are briefer than for CR 1936 and CR 1964 (cf. Figure 4). Specifically, only 59 inversions were observed, and only three inversion events lasted 4–5 h. Table 2 shows that the mapping predicts 62 individual inversion events, with both misses (FN = 15; e.g., 10–12 and 16 March) and excesses (FP = 18; e.g., 19 March and 1 April). Quantitatively, POD = 0.75 and FAR = 0.29, so three quarters of the observed inversions are predicted correctly and <30% of the predicted inversions are not observed. These and the other measures (e.g., skill scores) in Table 2 indicate better performance of the mapping for CR 1947 than for CR 1936 and CR 1964.

For CR 2016, Figure 6c and Table 2 show observational results similar to CR 1947: there are 53 individual inversion samples with most being brief. Table 2 also shows that our mapping predicts similar FN (=16) to, and smaller TP (=37) and larger FP (=30) than, those for CR 1947. The mapping performance is thus not as good as for CR 1947, e.g., POD = 0.70, SR = 0.55, and HK = 0.65 which are smaller than, and FAR = 0.45 and BS = 1.26 which are larger than, respectively, those for CR 1947 (and for CR 1964 as well).

Figure 6d and Table 2 show that for CR 2071 in the solar minimum phase of solar cycle 23, inversions are observed less often than in the other four rotations. Actually, only 35 samples are observed to be inversions, corresponding to 5.4% of the total hourly samples and less than half of the inversion events in CR 1936 and CR 1964. In addition, all these observed inversions have short durations of 1 or 2 h, a feature distinctly different from the other four rotations. Table 2 shows lower values of the verification metrics for CR 2071, e.g., POD = 0.69, SR = 0.34, and TS = 0.29, than those for CR 1947, CR 1964, and CR 2016. Nevertheless, the values of the skill scores HK = 0.61 and HSS = 0.41 still indicate that our predictions perform much better than random chance.

In summary, the verification metrics in Table 2 show consistent performance for the four rotations in the rising, solar maximum, and declining phases, while for CR 2071 in the solar minimum phase the performance is less satisfactory.

#### 5.2.2. Effects of the Undetermined Field Configurations

Table 2 shows that for CR 2071 the number of undetermined field configurations is significant at the level of 45%, much greater than 10%–25% for the other rotations. This great increase in the number of samples with undetermined field configurations for CR 2071 may be due to instrumental effects and/or orbital effects of the ACE spacecraft [*Owens et al.*, 2013]. If we assume, as for CR 1964 in section 5.1.3.2, that the observationally undetermined field configurations at the times of predicted inversions are indeed inversions, then POD = 0.86, SR = 0.93, TS = 0.80, HK = 0.85, and HSS = 0.88, corresponding to a great improvement in performance.

Adopting the same assumption, Table 2 shows that for CR 1936, CR 1947, and CR 2016, SR is improved to reach at least 80% and HK and HSS both are greater than 70%. Thus, provided that these undetermined observational field configurations are indeed inversions when predicted by the mapping, Table 2 shows consistently excellent performance of our mapping for all five rotations.

## 6. Discussion and Conclusions

To the best of our knowledge, this is the first time that field inversions have been studied in quantitative detail with a ballistic mapping technique, which neglects dynamic effects and assumes that the solar wind plasma

has a solar/coronal origin and flows at a constant speed [e.g., *Snyder and Neugebauer*, 1966; *Schatten et al.*, 1968; *Nolte and Roelof*, 1973; *Neugebauer et al.*, 2000; *MacNeice et al.*, 2011]. The mapping has been applied to five solar rotations across the different phases of solar cycle 23. For the four rotations in the rising, solar maximum, and declining phases, ≈65%–75% (=POD) of the observed inversions are predicted correctly and consistently and 55%–70% (=SR) of the predicted events are observed. Moreover, for these four rotations both the HK and HSS skill scores are >0.6, so our predictions perform much better than by random chance. For CR 2071 in the minimum phase of the solar cycle, the metrics are, e.g., POD = 0.69 and HK = 0.61 which are similar to, and SR = 0.34 and HSS = 0.41 which are lower than, those for the other four rotations. The overall performance of our predictions for CR 2071 is thus less satisfactory than for the other rotations.

Our mapping approach is based on a 2-D solar wind model with intrinsic nonradial magnetic fields [$B_\phi(\mathbf{r}_s)$] at the solar wind's source surface [*Schulte in den Bäumen et al.*, 2011, 2012] and otherwise almost identical elements to Parker's spiral model, which cannot predict fine inversion structures but can predict large-scale open fields for limited ranges of the in-ecliptic magnetic field angle. The generally very good quantitative agreement between our 2-D mapping approach and the observations for both short-duration (1–2 h) and longer-lasting inversions (see also Figures 4 and 6) suggests the following:

1. The intrinsic $B_\phi(\mathbf{r}_s)$ in (8) is important for the predicted inversions, which agree with most of the observations at 1 AU. In addition, most of the predicted inverted field lines follow the corotation direction and seldom oppose it.
2. The majority of the observed inversions are of solar/coronal origin, since in our model the solar wind originates from the source surface and has no subsequent dynamical interactions. This result is consistent with previous observational interpretations [e.g., *Crooker et al.*, 2004b; *Owens et al.*, 2013] and more advanced modeling [*Owens et al.*, 2013].
3. The 2-D mapping often captures well the most important features of the actual 3-D field, including the field topology (configurations) and local (at 1 AU) inversion structures, whose 3-D character is indicated by out-of-ecliptic magnetic field angles $|\theta_B| \overset{>}{\sim} 45°$ (see Figure 1) and is proposed to be important for long-lasting inversions [*Crooker et al.*, 2004b].

As discussed in *Owens et al.* [2013], over the entire 1998–2011 interval there is a significant fraction (30%) of observation periods when the configurations of the magnetic field cannot be determined. Notably, the undetermined fraction amounts to almost half (45%) during CR 2071, much higher than <25% for the other three rotations. The large fraction of undetermined field configurations for CR 2071 may be one factor that limits the performance of our mapping. The performance measures would be POD = 0.86, SR = 0.93, HK = 0.85, and HSS = 0.88, for instance, corresponding to excellent agreement between predictions and observations, if observationally undetermined configurations at the times of predicted inversions are assumed to actually be inversions. The same assumption for all the other four rotations also improves the performance metrics, leading to consistent values for all the five rotations. These values plausibly indicate the best level of performance that our mapping can achieve.

Interestingly, the inversions in CR 2071 show a distinct feature in terms of duration: all the observed inversion events in CR 2071 are short, with durations of 1 or 2 h, while longer-lasting inversions are observed in the other four rotations. Short 1–2 h inversions are proposed to be caused at least partly by turbulent processes [*Owens et al.*, 2013] and longer-lasting inversions by interchange reconnection near the Sun [*Crooker et al.*, 2004b; *Owens et al.*, 2013]. Since magnetic structures associated with turbulence are plausibly more variable than those due to reconnection [*Owens and Forsyth*, 2013], our mapping's assumption of constant wind over one rotation is expected to be less satisfactory for field structures associated with turbulence than for reconnection. Consequently, the possibly larger role for turbulence in forming the inversions in CR 2071 may be another factor that limits our prediction performance relative to the other rotations.

Although large-scale field configurations are not the focus of this work, the mapping also shows that our predictions agree with, for CR 1964, 85% of the hourly data, surpassing Parker's spiral model by 15% (see section 5.1.4). For the other four solar rotations across solar cycle 23, our mapping predicts correctly 72%–78% of the observed field configurations, better than Parker's model by 5%–8%. The mapping success rates here are somewhat lower than those for two other solar rotations studied in our previous work [*Li et al.*, 2016a], where the mapping predicted successfully ≈90% of the observed field configurations, exceeding Parker's model by ≈20%. The differences may be because the PAD data are processed differently in the works of *Owens et al.* [2013] and *Li et al.* [2016a], with the PAD classes being identified automatically
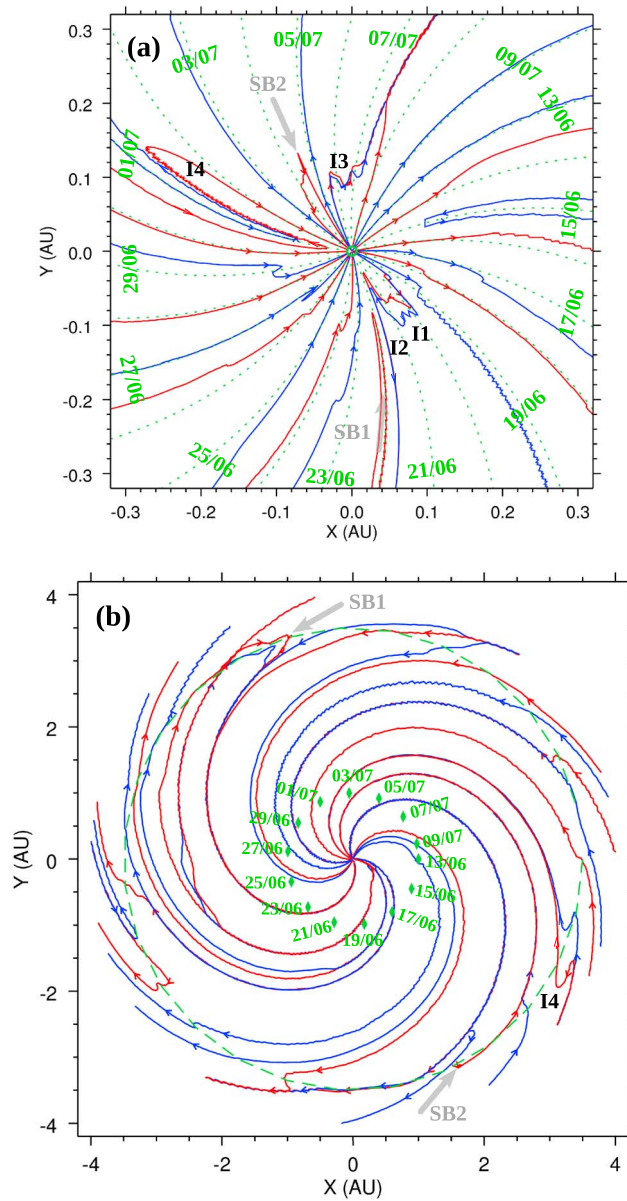
**Figure 7.** Predicted maps of magnetic field lines for CR 1964. The starting points for the mapping are spaced at longitudes corresponding to 0000 UT each day on Earth and at heliocentric distances (a) $r = 0.1$ AU and (b) $r = 3.5$ AU, with otherwise identical conditions to Figure 2. The black labels I1–I4 have same meanings as in Figure 2.

and manually, respectively. Moreover, the PAD class called heat flux dropouts, usually a proxy for loops disconnected from the Sun [e.g., *McComas et al.*, 1989; *Owens and Crooker*, 2007], was not included in the classifications of *Owens et al.* [2013] except in the undetermined class.

Our approach assumes constant solar wind over one solar rotation, with wind properties varying in radial distance and longitude (except for the wind speed which varies with longitude only). This assumption can be improved by using solar wind observations from multiple spacecraft (e.g., STEREO and ACE) in the future, in order to reduce the duration of the interval in which constant solar wind conditions are assumed. In addition, our approach approximates the divergence-free condition $\nabla \cdot \mathbf{B} = 0$ in two ways. First, the azimuthal gradients in $B_\phi$ are neglected in deriving (5), which thus assumes conservation of the radial magnetic flux; this is supported by observations near Earth [*Owens et al.*, 2008] and is largely justified by the model results [*Li et al.*, 2016a]. Second, the mapping (1)–(4) does not explicitly impose the divergence-free requirement. Nonetheless, *Li et al.* [2016a] demonstrated that our mapping predictions agree well with PAD data, which suggests that the mapping approximation is valid most of the time. Note also that our assumption that PAD classes are good proxies for magnetic field configurations may not always hold. For example, counter-streaming strahls at both 0° and 180° pitch angles can develop on open field lines, due to concurrent magnetic connections to the Sun in one direction and to Earth's bow shock or other magnetic structures in the other direction [e.g.,

*Wimmer-Schweingruber et al.*, 2006]. This assumption may have nonnegligible effects on the comparison between our predictions and the observations, as discussed in *Li et al.* [2016a].

In the future, it will be interesting to study inversions at other heliocentric distances and the associated variation with $r$ of inversion occurrence rate, using solar wind data from spacecraft both near Earth and farther away (e.g., Helios, Juno, Messenger, and Ulysses) and our mapping approach. It has been shown in this work that inversions are one of the interplanetary signatures of the intrinsic $B_\phi$ at the source surface. Other signatures include the presence of magnetic loops and nonspiral structures like radial field, see section 5.1.2. Our model predicts, as does Parker's model, that $B_r$ decreases as $1/r^2$ for $r \gg r_s$, while $B_\phi$ decreases as $1/r$, as seen from (5) and (6). The intrinsic $B_\phi(\mathbf{r}_s)$ source and these different $r$ dependences for $B_r$ and $B_\phi$ may have important effects on whether or not inversions can be formed at a given $r$. For example, inversions are expected to

disappear for sufficiently large $r$ ($\gg$ 1 AU) in the outer heliosphere where the field lines are primarily azimuthal and at sufficiently small $r$ where the field lines are essentially radial.

As an illustration, Figures 7a and 7b show two maps of predicted field lines, where the starting points of the mapping are at $r = 0.1$ AU and $r = 3.5$ AU, respectively, and other conditions are the same as for Figure 2. We see from Figure 7a that field line inversions often occur near 0.1 AU, as for the blue and red lines labeled I1–I3, and sometimes farther out near 0.3 AU, like the red field line labeled I4; here I1–I4 correspond to the labels in Figure 2. Figure 7b shows that farther away from Earth's orbit field lines are more tightly wound than within Earth's orbit and that inversions are only seen near 3.5 AU at the longitudes corresponding to the inversion I4 in Figure 2. We found that the ratio $|B_\phi(r)/B_r(r)|$ increases substantially between 0.1 AU and 3.5 AU: from around 0.1 at 0.1 AU, increasing to $\approx 1$ for a significant fraction of longitudes near 1 AU, and to above 1 often reaching $\approx 10$ at 3.5 AU. These results thus demonstrate that for inversions to take place, in addition to the requirement of sign changes in $\mathbf{B}_r$, the $B_\phi$ component relative to $B_r$ has to be large enough yet not too large.

Finally, the successful applications of our mapping technique to most of the field inversions and field configurations observed at 1 AU for six solar rotations to date suggest that the mapping approach is robust and well suited for predicting in the future the connectivity to Earth of SEPs, in addition to solar wind strahl electrons.

## References

Balogh, A., R. J. Forsyth, E. A. Lucek, T. S. Horbury, and E. J. Smith (1999), Heliospheric magnetic field polarity inversions at high heliographic latitudes, *Geophys. Res. Lett.*, *26*, 631–634.

Burlaga, L. F., and N. F. Ness (1993), Large-scale distant heliospheric magnetic field: Voyager 1 and 2 observations from 1986 through 1989, *J. Geophys. Res.*, *98*, 17,451–17,460.

Crooker, N. U., M. E. Burton, G. L. Siscoe, S. W. Kahler, J. T. Gosling, and E. J. Smith (1996), Solar wind streamer belt structure, *J. Geophys. Res.*, *101*, 24,331–24,341.

Crooker, N. U., C.-L. Huang, S. M Lamassa, D. E. Larson, S. W. Kahler, and H. E. Spence (2004a), Heliospheric plasma sheets, *J. Geophys. Res.*, *109*, A03107, doi:10.1029/2003JA010170.

Crooker, N. U., S. W. Kahler, D. E. Larson, and R. P. Lin (2004b), Large-scale magnetic field inversions at sector boundaries, *J. Geophys. Res.*, *109*, A03108, doi:10.1029/2003JA010278.

Erdős, G. A. N., and A. Balogh (2014), Magnetic flux density in the heliosphere through several solar cycles, *Astrophys. J.*, *781*, 50.

Fainberg, J., and R. G. Stone (1974), Satellite observations of type III solar radio bursts at low frequencies, *Space Sci. Rev.*, *16*, 145–188.

Fainberg, J., L. G. Evans, and R. G. Stone (1972), Radio tracking of solar energetic particles through interplanetary space, *Science*, *178*, 743–745.

Fazakerley, A. N., L. K. Harra, and L. van Driel-Gesztelyi (2016), An investigation of the sources of Earth-directed solar wind during Carrington rotation 2053, *Astrophys. J.*, *823*, 145.

Feldman, W. C., J. R. Asbridge, S. J. Bame, M. D. Montgomery, and S. P. Gary (1975), Solar wind electrons, *J. Geophys. Res.*, *80*, 4181–4196.

Foullon, C., et al. (2009), The apparent layered structure of the heliospheric current sheet: Multi-spacecraft observations, *Sol. Phys.*, *259*, 389–416.

Gosling, J. T., D. N. Baker, S. J. Bame, W. C. Feldman, R. D. Zwickl, and E. J. Smith (1987), Bidirectional solar wind electron heat flux events, *J. Geophys. Res.*, *92*, 8519–8535.

Jokipii, J. R., and J. Kota (1989), The polar heliospheric magnetic field, *Geophys. Res. Lett.*, *16*, 1–4.

Kahler, S., and R. P. Lin (1994), The determination of interplanetary magnetic field polarities around sector boundaries using $E > 2$ keV electrons, *Geophys. Res. Lett.*, *21*, 1575–1578.

Kahler, S., and R. P. Lin (1995), Examination of directional discontinuities and magnetic polarity changes around interplanetary sector boundaries using >2 keV electrons, *Sol. Phys.*, *161*, 183–195.

Kahler, S., N. U. Crooker, and J. T. Gosling (1996), The topology of intrasector reversals of the interplanetary magnetic field, *J. Geophys. Res.*, *101*, 24,373–24,382.

Kahler, S., N. U. Crooker, and J. T. Gosling (1998), Properties of interplanetary magnetic sector boundaries based on electron heat-flux flow directions, *J. Geophys. Res.*, *103*, 20,603–20,612.

Li, B., I. H. Cairns, J. T. Gosling, G. Steward, M. Francis, D. Neudegg, H. Schulte in den Bäumen, P. R. Player, and A. R. Milne (2016a), Mapping magnetic field lines between the Sun and Earth, *J. Geophys. Res. Space Physics*, *121*, 925–948, doi:10.1002/2015JA021853.

Li, B., I. H. Cairns, J. T. Gosling, D. M. Malaspina, D. Neudegg, G. Steward, and V. V. Lobzin (2016b), Comparisons of mapped magnetic field lines with the source path of the 7 April 1995 type III solar radio burst, *J. Geophys. Res. Space Physics*, *121*, 6141–6156, doi:10.1002/2016JA022756.

Liu, Y. C.-M., et al. (2014), A statistical analysis of heliospheric plasma sheets, heliospheric current sheets, and sector boundaries observed in situ by STEREO, *J. Geophys. Res. Space Physics*, *119*, 8721–8732.

Lockwood, M. (2013), Reconstruction and prediction of variations in the open solar magnetic flux and interplanetary conditions, *Living Rev. Sol. Phys.*, *10*, 4.

Lockwood, M., M. J. Owens, and A. P. Rouillard (2009), Excess open solar magnetic flux from satellite data: 2. A survey of kinematic effects, *J. Geophys. Res.*, *114*, A11104, doi:10.1029/2009JA014450.

Lockwood, M., H. Nevanlinna, L. Barnard, M. J. Owens, R. G. Harrison, A. P. Rouillard, and C. J. Scott (2014), Reconstruction of geomagnetic activity and near-Earth interplanetary conditions over the past 167 yr — Part 4: Near-Earth solar wind speed, IMF, and open solar flux, *Ann. Geophys.*, *32*, 383–399.

MacNeice, P., B. Elliott, and A. Acebal (2011), Validation of community models: 3. Tracing field lines in heliospheric models, *Space Weather*, *9*, S10003, doi:10.1029/2011SW000665.

McComas, D. J., J. T. Gosling, J. L. Phillips, S. J. Bame, J. G. Luhmann, and E. J. Smith (1989), Electron heat flux dropouts in the solar wind: Evidence for interplanetary magnetic field reconnection?, *J. Geophys. Res.*, *94*, 6907–6916.

Neugebauer, M. (2008), Heliospheric sector boundaries: Single or multiple?, *J. Geophys. Res.*, *113*, A12106, doi:10.1029/2008JA013453.

Neugebauer, M., E. J. Smith, A. Ruzmaikin, J. Feynman, and A. H. Vaughan (2000), The solar magnetic field and the solar wind: Existence of preferred longitudes, *J. Geophys. Res.*, *105*, 2315–2324.

Nolte, J. T., and E. C. Roelof (1973), Large-scale structure of the interplanetary medium, I: High coronal source longitude of the quiet-time solar wind, *Sol. Phys.*, *33*, 241–257.

Owens, M. J., and N. U. Crooker (2007), Reconciling the electron counterstreaming and dropout occurrence rates with the heliospheric flux budget, *J. Geophys. Res.*, *112*, A06106, doi:10.1029/2006JA012159.

Owens, M. J., and R. Forsyth (2013), The heliospheric magnetic field, *Living Rev. Sol. Phys.*, *10*, 5.

Owens, M. J., C. N. Arge, N. U. Crooker, N. A. Schwadron, and T. S. Horbury (2008), Estimating total heliospheric magnetic flux from single-point in situ measurements, *J. Geophys. Res.*, *113*, A12103, doi:10.1029/2008JA013677.

Owens, M. J., N. U. Crooker, and M. Lockwood (2013), Solar origin of heliospheric magnetic field inversions: Evidence for coronal loop opening within pseudostreamers, *J. Geophys. Res. Space Physics*, *118*, 1868–1879, doi:10.1002/jgra.50259.

Parker, E. N. (1958), Dynamics of the interplanetary gas and magnetic fields, *Astrophys. J.*, *128*, 664.

Reiner, M. J., J. Fainberg, and R. G. Stone (1995), Large-scale interplanetary magnetic field configuration revealed by solar radio bursts, *Science*, *270*, 461–464.

Richardson, I. G., and H. V. Cane (2010), Near-Earth interplanetary coronal mass ejections during solar cycle 23 (1996–2009): Catalog and summary of properties, *Sol. Phys.*, *264*, 189–237.

Rosenbauer, H., R. Schwenn, E. Marsch, B. Meyer, H. Miggenrieder, M. D. Montgomery, K. H. Muehlhaeuser, W. Pilipp, W. Voges, and S. M. Zink (1977), A survey on initial results of the Helios plasma experiment, *J. Geophys. Z. Geophys.*, *42*, 561–580.

Schatten, K. H., N. F. Ness, and J. M. Wilcox (1968), Influence of a solar active region on the interplanetary magnetic field, *Sol. Phys.*, *5*, 240–256.

Schulte in den Bäumen, H., I. H. Cairns, and P. A. Robinson (2011), Modeling 1 AU solar wind observations to estimate azimuthal magnetic fields at the solar source surface, *Geophys. Res. Lett.*, *38*, L24101, doi:10.1029/2011GL049578.

Schulte in den Bäumen, H., I. H. Cairns, and P. A. Robinson (2012), Nonzero azimuthal magnetic fields at the solar source surface: Extraction, model, and implications, *J. Geophys. Res.*, *117*, A10104, doi:10.1029/2012JA017705.

Snyder, C. W., and M. Neugebauer (1966), The relation of Mariner-2 plasma data to solar phenomena, in *The Solar Wind*, edited by R. J. Mackin, and M. Neugebauer, pp. 25–32, Pergamon Press, Oxford, U. K.

Solanki, S. K., B. Inhester, and M. Schüssler (2006), The solar magnetic field, *Rep. Prog. Phys.*, *69*, 563–668.

Stanski, H, L. J. Wilson, and W. R. Burrows (1989), Survey of common verification methods in meteorology, *Res. Rep. No. MSRB 89-5*, Atmos. Environ. Serv., Ontario, Can.

Suzuki, S., and G. A. Dulk (1985), Bursts of type III and type V, in *Solar Radiophysics*, edited by D. J. McLean, and N. R. Labrum, pp. 289–332, Cambridge Univ. Press, Cambridge, U. K.

Szabo, A., D. E. Larson, and R. P. Lepping (1999), The heliospheric current sheet on small scale, in *Solar Wind Nine*, vol. 471, edited by S. Habbal et al., pp. 589–592, Am. Inst. of Phys., College Park, Md.

Thomas, B. T., and E. J. Smith (1980), The Parker spiral configuration of the interplanetary magnetic field between 1 and 8.5 AU, *J. Geophys. Res.*, *85*, 6861–6867.

Wimmer-Schweingruber, R. F., et al. (2006), Understanding interplanetary coronal mass ejection signatures, *Space Sci. Rev.*, *123*, 177–216.

Woodcock, F. (1976), The evaluation of yes/no forecasts for scientific and administrative purposes, *Mon. Weather Rev.*, *104*, 1209–1214.

Zurbuchen, T. H., and I. G. Richardson (2006), In-situ solar wind and magnetic field signatures of interplanetary coronal mass ejections, *Space Sci. Rev.*, *123*, 31–43.